

18 **Abstract**

19 In continuous permafrost regions, pathways for transport of sub-permafrost groundwater to the
20 surface sometimes perforate the frozen ground and result in the formation of a pingo.
21 Explanations offered for the locations of such pathways have so far included hydraulically
22 conductive geological units and faults. On Svalbard, several pingos locate at valley flanks where
23 these controls are apparently lacking. Intrigued by this observation, we elucidated the geological
24 setting around such a pingo with electrical resistivity tomography. The inverted resistivity
25 models showed a considerable contrast between the uphill and valley-sides of the pingo. We
26 conclude that this contrast reflects a geological boundary between low-permeable marine
27 sediments and consolidated strata. Groundwater presumably flows towards the pingo spring
28 through glacially induced fractures in the strata immediately below the marine sediments. Our
29 finding suggests that flanks of uplifted Arctic valleys deserve attention as possible discharge
30 locations for deep groundwater and greenhouse gasses to the surface.

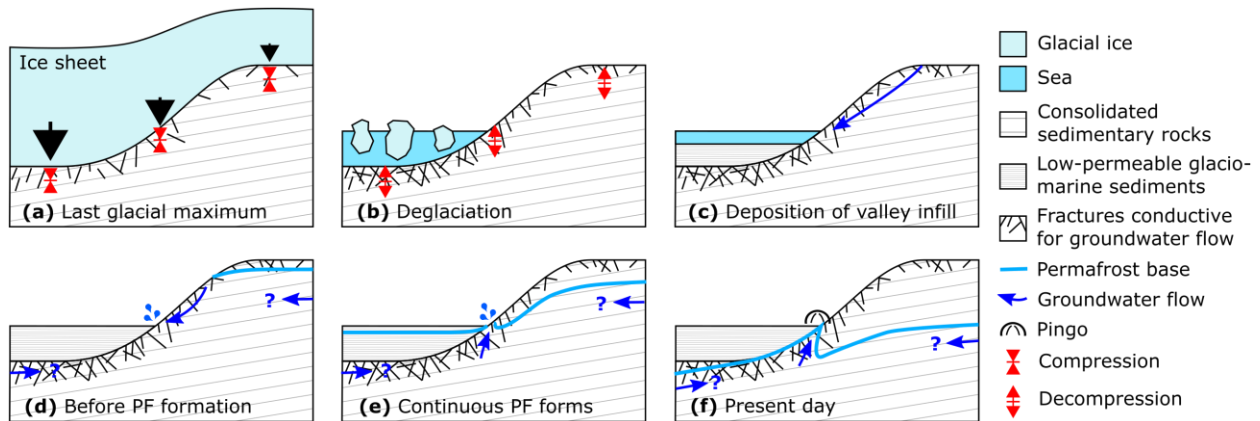
31 **1 Introduction**

32 In continuous permafrost regions, several deep (sub-permafrost) groundwater systems
33 have shown to be artesian and to host considerable amounts of methane and carbon dioxide
34 (Hodson et al., 2019, 2020; Huq et al., 2017). Continuous permafrost separates deep groundwater
35 and other fluids from the atmosphere, but exchange to and from shallower depths may still take
36 place if taliks (i.e., locally unfrozen ground) perforate the frozen ground (i.e., a through-talik). In
37 a warming climate, permafrost thaw alters the hydrogeological conditions, and transfer rates of
38 methane, CO₂ and other substances are expected to increase (Grosse et al., 2016; Schuster et al.,
39 2018). We need to understand the present hydrological setting in order to quantify the potential
40 impact of anthropogenic global warming upon fluid migration in the Arctic,

41 Perennial springs in the High Arctic exemplify through-taliks that carry groundwater
42 (hereafter ‘active through-taliks’) towards the ground surface (Andersen et al., 2002; Grasby et
43 al., 2012; Haldorsen et al., 1996; Williams, 1970). A pingo (i.e., an ice-cored hill) forms when
44 this spring discharge freezes below the thaw-protecting active layer (Mackay, 1998). By
45 definition, this pingo will be of the open-system type because it is fed by groundwater not
46 enclosed by permafrost (Liestøl, 1996). Pingos persist for as long as permafrost conditions
47 remain, and even so after the through-talik has potentially frozen over and the spring discharge
48 has ceased. Consequently, open-system pingos indicate current or previous presence of active
49 through-taliks (Yoshikawa, 2013).

50 Both active through-taliks and open-system pingos require artesian pressure in the sub-
51 permafrost groundwater system (French, 2017). In areas of continuous permafrost, such
52 pressures may be produced by recharge from glacial meltwater infiltrating the ground below
53 warm-based glaciers (e.g., Liestøl, 1977; Scheidegger & Bense, 2014) or, where permafrost is
54 relatively young, by freezing expansion associated with basal permafrost aggradation (Hornum et
55 al., 2020). While artesian pressure is a prerequisite for the transport of deep groundwater towards
56 the surface, a sufficiently hydraulically conductive pathway is also needed. Permeable geological
57 units (e.g., Haldorsen et al., 1996) and faults (e.g., Rossi et al., 2018; Scheidegger et al., 2012;
58 Scholz & Baumann, 1997; Z. Wu et al., 2005) comprise the current examples of such migration
59 pathways.

60 In Svalbard, many pingos are found along valley flanks (Humlum et al., 2003), and
 61 several of these occur where no links to hydraulically conductive geological units or faults are
 62 known (Ballantyne, 2018). We propose that that a combination of low-permeability Holocene
 63 marine sediments and underlying fractures resulting from pre-Holocene glacial loading and
 64 unloading may constitute a previously overseen explanation for springs located at valley
 65 margins. Figure 1 illustrates our conceptual model for spring formation at valley margins with
 66 cross-sections of the side of a typical glacially-cut valley on Svalbard ranging from glaciation to
 67 present day conditions. During the various glaciation cycles, glacial loading and unloading has
 68 caused ground compression and decompression along with fracturing (Figure 1a–b; e.g., Neuzil,
 69 2012). Glacial fracturing of the subsurface is likely most abundant within the valleys, because of
 70 the greater pressures generated here (Leith et al., 2014a, 2014b). Following deglaciation, low-
 71 permeability marine and deltaic sediments are deposited on top of the fracture zone (Gilbert et
 72 al., 2018), confining groundwater flow (Figure 1c). Given the right conditions, a spring forms at
 73 the end of the hill slope (Figure 1d, Fitts, 2002) when the sea retreats. In Late Holocene,
 74 temperatures drop to form continuous permafrost (Humlum, 2005; Mangerud & Svendsen,
 75 2017), but the ground stays unfrozen below the spring site due to hydrological advective heat
 76 transfer (Figure 1e). As permafrost thickness increases, the active through-talik forms along the
 77 fractured zone, because it comprises the most hydraulically conductive pathway (Figure 1f).



78
 79 **Figure 1** Cross sections of a typical valley on Svalbard showing our conceptual model of why
 80 many pingos locate at valley margins (Figure 2). **a)** and **b)** Glacial loading (a) and unloading (b),
 81 respectively, causes compression and decompression of the ground and results in fracturing
 82 (Leith et al., 2014a, 2014b). The fractures produced this way are more abundant below valley
 83 bottoms. **c)** Low-permeable marine and deltaic sediments are deposited in the fjord valley
 84 (Gilbert et al., 2018) constituting and low-permeable cover on top of the conductive fracture
 85 zone. **d)** After relative sea-level fall, a spring forms at the end of hill slope. **e)** Continuous
 86 permafrost forms, but the ground stays unfrozen below the spring site due to advective heat
 87 transfer. **f)** Comprising the most hydraulically conductive pathway, groundwater is transported
 88 towards the spring along the fractured layer.

89 Surface-based electrical methods have been widely used to map and characterize frozen
 90 and unfrozen ground in permafrost environments (Kneisel et al., 2008). In most locations, frozen
 91 ground can be expected to have a significantly higher electrical resistivity (>1000 Ωm , Kneisel &
 92 Hauck, 2008) than unfrozen (<500 Ωm , Palacky, 1988). However, clay-rich and saline
 93 permafrost environments may possess significantly lower resistivities. Frozen clay and other

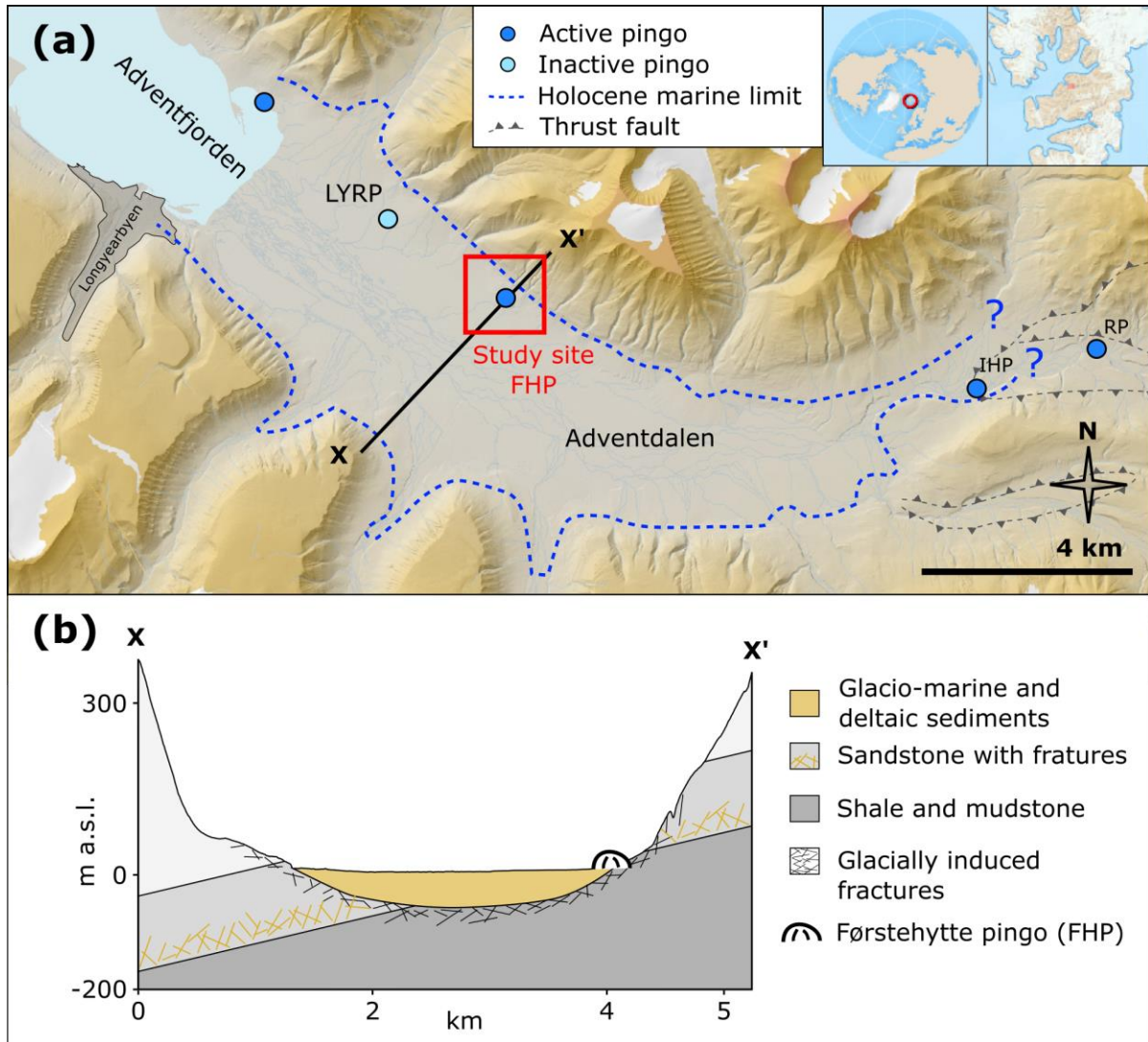
94 fine-grained sediments can host microfilms of unfrozen water even at temperatures below -5 °C
95 (Scott et al., 1990) and show electrical resistivities below 100 Ωm (Harada & Yoshikawa, 1996;
96 Keating et al., 2018; Minsley et al., 2012). Upon ground freezing, groundwater brinification may
97 take place as solutes are expelled to the residual water (Cochand et al., 2019). Saline, unfrozen,
98 and electrically conductive groundwater may occur as microfilms within frozen ground (Keating
99 et al., 2018) or as larger inclusions (i.e., cryopegs; Gilbert et al., 2019; Gilichinsky et al., 2003).

100 We investigate the above conceptual model by elucidating the geological and
101 hydrogeological context at the margins of a valley-flank, active open-system pingo by measuring
102 the electrical resistivity in the ground.

103 **2 Study site**

104 The study site was Førstehytte Pingo (FHP), one of five open-system pingos in Lower
105 Adventdalen, found in central Spitsbergen, the biggest island in the Svalbard archipelago (Figure
106 2a). As for the rest of Svalbard, continuous permafrost dominates Adventdalen due to a cold and
107 dry climate. Permafrost thicknesses range from <200 m in the valley floor to >450 m in the
108 adjacent mountains (Christiansen et al., 2005; Humlum et al., 2003; Liestøl, 1977). With one
109 exception, all five pingos are active and perennially discharge brackish methane-rich waters in
110 orders of 10^{-1} L s⁻¹ (Hodson et al., 2019, 2020; Hornum et al., 2020; Liestøl, 1977; Yoshikawa,
111 1993; Yoshikawa & Nakamura, 1996). The chemistry of the spring discharge shows that all
112 pingos relate to a regional sub-permafrost groundwater system (Hodson et al., 2020; Hornum et
113 al., 2020). The two most up-valley pingos, Innerhytte (IHP) and River (RP) pingos, have formed
114 in fractured shale and their positions are likely explained by an underlying fault that constitutes a
115 hydraulically conductive pathway (Figure 2a, Rossi et al., 2018). Moving westwards into the
116 lowest part of Adventdalen, FHP is the first of three pingos (the other two being Longyear,
117 LYRP, and Lagoon, LP, pingos) that all have formed in Holocene marine muds (Yoshikawa &
118 Harada, 1995), but locate close to the boundary to well-consolidated sedimentary rock (Figure
119 2b). All three align with the Northeastern flank of Adventdalen and the elongated shapes of LP
120 and FHP are both parallel with this alignment.

121 Below the valley floor of Adventdalen, an up 60 m thick succession of Late Weichselian
122 to Holocene glacio-marine and deltaic sediments overlies well-consolidated rocks of Cretaceous
123 age or older (Figure 2, Gilbert et al., 2018). Together, all units comprise a groundwater system
124 with a very low permeability, and most fluid flow is restricted to fractures in the consolidated
125 bedrock. Such fractures are found in particular stratigraphic units (Figure 2b, Olausen et al.,
126 2020, and references therein) and in the consolidated sedimentary rock immediately below
127 glacio-marine succession (Figure 2b, Gilbert et al., 2018). Fractures in the latter are likely of
128 glaciogenic origin (e.g., Neuzil, 2012).



129

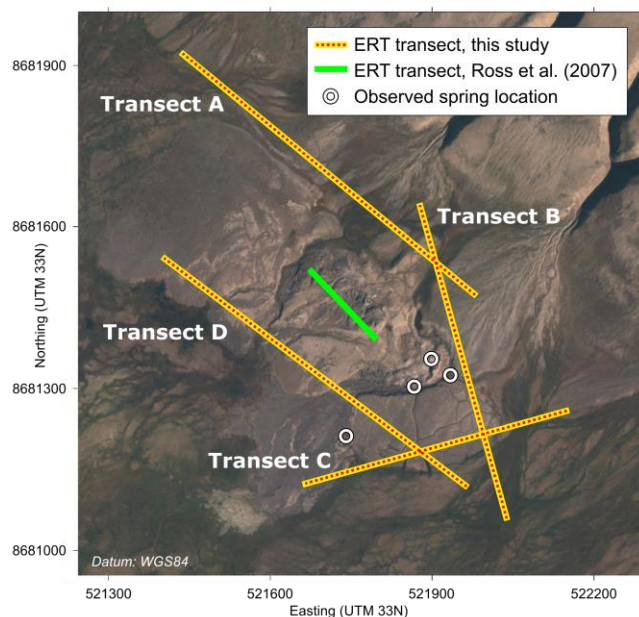
130 **Figure 2 a)** Overview of Lower Adventdalen that shows the location of pingos, the study site
 131 (red square), and the Holocene marine limit. Topographic data used to create the map by
 132 courtesy of Norwegian Polar Institute (2020). **b)** Geological cross-section across Adventdalen
 133 and the study site. Fractures in the sandstone unit and below the succession of glacio-marine and
 134 deltaic sediments interrupt the dominant low-permeability of the groundwater system. Cross-
 135 section modified from Hodson et al., 2020).

136 **3 ERT - Data collection and processing**

137 Measurements of direct current (DC) resistivity in the ground below FHP were carried
 138 out along four 2D transects through electrical resistivity tomography (ERT) surveying
 139 implementing the Wenner- α configuration (cf., Reynolds, 2011) during three weeks in
 140 September 2017 (Figure 3). At this time of year, the thawed active layer allowed for easy
 141 installation of electrodes and good electrical connectivity with the ground. The ERT surveys
 142 were performed with an ABEM-SAS-1000 Terrameter coupled with an ABEM-ES10-64
 143 Electrode Selector. The layout for a single survey consisted of four cables in a roll-along
 144 configuration, each with 21 electrode take-outs and an electrode spacing of 5 m. Only uneven

145 electrode take-outs were used and the last takeout on a cable was aligned with the first takeout on
146 the subsequent one so that the combined cable was 400 m long and connected to 41 stainless
147 steel electrodes. All possible four-electrode Wenner- α configurations were measured in both
148 normal and reciprocal mode to reduce measurement error (Binley & Kemna, 2005; Kim et al.,
149 2016). This resulted in 260 unique electrode configurations and a maximum of 520
150 measurements for each line. Less measurements were available when electrodes were left out
151 due to bad connectivity to the ground. The current induced to the ground varied between 200–
152 1000 mA. Thirteen surveys were carried out along the four transects covering most of the pingo
153 margin (Figure 3). At each transect, two to four surveys were undertaken and provided ca. 300 m
154 overlap between consecutive surveys. This resulted in total transect lengths of 500, 600 or 700
155 m, respectively comprising 375, 490 and 605 unique electrode configurations.

156 Electrode positions were mapped with a handheld GPS device (Garmin GPSMAP®
157 76C). When measuring the coordinate position within a limited time (<1 hr), this device showed
158 to have a relatively high precision (<0.1 m) but low accuracy (<2 m). We adjusted for the low
159 accuracy by noting particular electrodes, whose locations could be accurately pinpointed on the
160 orthomap (Figure 3) and translated the coordinates accordingly. Because of the relatively poor
161 vertical precision of handheld GPS measurements, we inferred the topography along the ERT
162 lines by projecting the electrode positions on a 5-m-resolution DEM of the field area (not shown,
163 Norwegian Polar Institute, 2020).



164
165 **Figure 3** Orthophoto of the study site at Førstehytte Pingo showing the location of the four ERT
166 transects from this study, the ERT transect from Ross et al. (2007) and observed spring locations.
167 The location of the study site is shown on Figure 2. Orthophoto by courtesy of Norwegian Polar
168 Institute (2020).

169 To ensure good quality of the resistivity data used for the inversion, we first performed
170 statistical data cleaning. The final product of this pre-processing was four files, one for each
171 transect, containing up to one measurement for each unique electrode configuration. Details of
172 the data pre-processing can be found in the Supporting Information (Text S1).

173 2D inversion of the measured apparent resistivities were carried out using the graphical
174 user interface (GUI) of ResIPy 3.0.1, an open-source software for inversion and modelling of
175 geoelectrical data (Blanchy et al., 2020). ResIPy builds on the R2 code (version 4.02, Binley,
176 2019) for the inversion of DC resistivities. We employed a triangular mesh for the inversion.
177 Following the default settings in the GUI of ResIPy, the mesh was composed of a fine mesh that
178 defined the region of the final resistivity model encompassed by a coarse mesh. The lateral
179 extent of the fine mesh was the transect length and the coarse mesh extended five times the
180 transect length to both sides. The fine-to-coarse mesh boundary was at 50 m b.g.l. and the coarse
181 mesh extended to a depth of 30% the total lateral mesh extent. The resolution of the fine mesh
182 was defined by a characteristic length of 4.38 and a growth factor of 4. This resulted in fine
183 meshes with 1705, 1490, 1582 and 1741 triangles for transects A, B, C and D, respectively. We
184 used the inversion type ‘normal regularization with linear filtering’ and the convergence criterion
185 was defined by a root-mean-square error (RMSE) of <1.2%. The certainty of the electrical
186 resistivities predicted by the inversion was quantified by sensitivity maps as calculated by the
187 default settings in ResIPy (Eq. 5.19 in Binley & Kemna, 2005). Sensitivity values below unity
188 indicate that inverted resistivities are weakly constrained by data. Similarly, higher values
189 indicate that inverted resistivities are well constrained by data and allows for greater faith in the
190 resistivity model.

191 All measured and inverted electrical resistivity data resulting from this research is public
192 available from the Zenodo repository (Hornum, 2021).

193 **4 Results**

194 Figure 4 shows the electrical resistivity models produced by the inversion of the
195 measured values and the sensitivity of the resistivity values predicted by these models. To
196 facilitate further spatial understanding, we also produced a 3D animation. In addition to the
197 resistivity models produced from our own survey, the animation also shows a resistivity model
198 from FHP presented by Ross et al. (2007). The animation is available as Supporting Information
199 (Movie S1).

200 The electrical resistivity models predicted significantly varying values and patterns at
201 different sides of FHP. Based on the differences of the predicted resistivity values, we divided
202 the transects into three segments (I, II, and III), which are summarized in Table 1 and described
203 in detail below.

204 Segment I covers transects A, B, and the eastern part of Transect C and situate between
205 FHP and the mountainside. The resistivity model show that the subsurface here generally is
206 characterized by high resistivity values that range from 1000 to 5000 Ωm . Relatively large and
207 elongated zones up to ~200 x 60 m (width x height) of very high resistivities (5000–50000 Ωm)
208 are also common, but these do not extend to depths shallower than ~10 m b.g.l.

209 Segment II possesses the most complex resistivity pattern of this survey. This segment
210 locates south of the southeastern end of FHP and covers the western part of Transect C and the
211 southeastern part of Transect D. In approximately the deepest 15 to 25 m, Segment II is
212 characterized by low resistivity values that range from 20 to 100 Ωm . A relatively sharp
213 boundary (<5 m) marks the transition to a lateral zone of moderate to high resistivity values
214 (500–5000 Ωm). This resistivity range generally dominates the shallowest 25–35 m of the
215 subsurface, but not at the boundary to Segment II (Transect C), where low resistivity values

216 extent to near the surface. The moderate to high resistivities are distributed in a heterogeneous
 217 way, and vary between the extreme ends of the range several times along the extent of Segment
 218 II.

219 Moving on to Segment III and the southwestern flank of FHP, a further decrease in the
 220 ground resistivity can be observed. Segment III covers the northwestern part of the Transect D
 221 and locates between FHP and the valley center. Low resistivity values of up to 50 Ωm
 222 characterize the lower part of Segment III and gradually decrease upwards to very low resistivity
 223 values of down to 1.8 Ωm . A sharp boundary can be observed in the shallow part of Segment III
 224 towards Segment II in the form of the contrasting resistivities, but at greater depths the resistivity
 225 values are close to identical in both segments.

226 Showing mostly logarithmic values above zero, the sensitivity maps on Figure 4 indicate
 227 that the majority of the inverted resistivity values are relatively well constrained by the
 228 measurements. The sensitivity map of Segment III forms an exception to this pattern by showing
 229 log-sensitivity values below zero except for in the shallowest cells. The predicted resistivities in
 230 Segment III were thus generally not well constrained by the measurements.

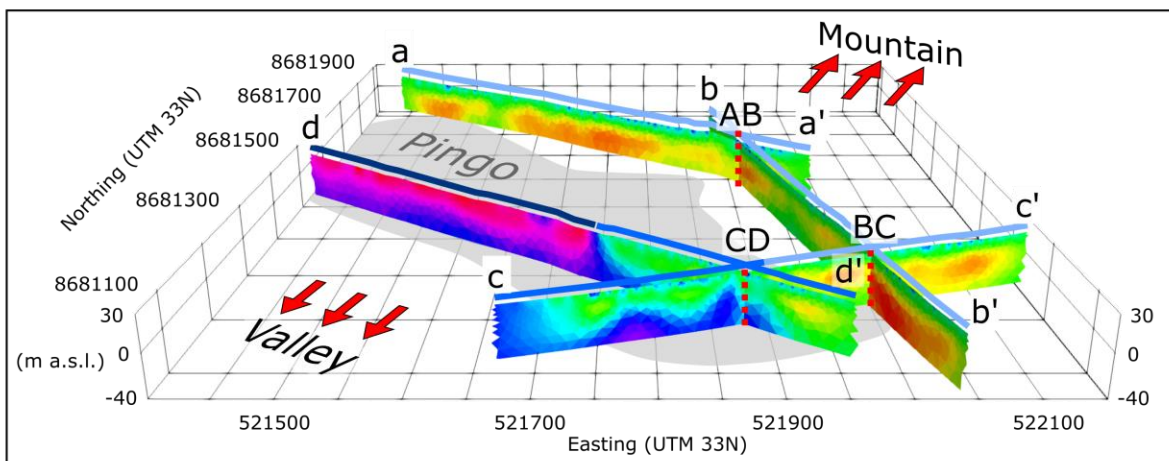
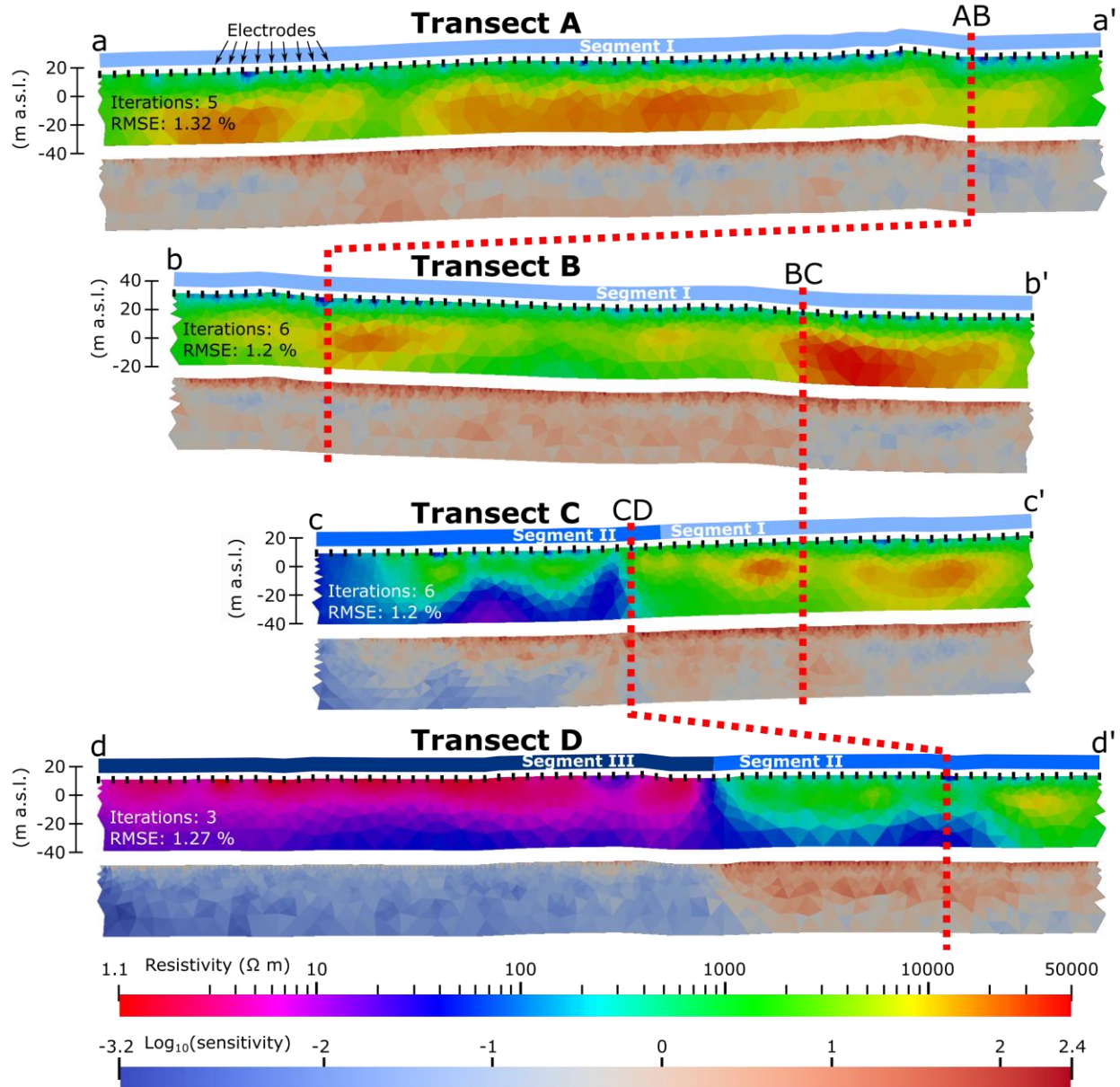
231 **Table 1** Summary of electrical resistivity patterns observed on the resistivity models (Figure 4).

	Segment A	Segment B	Segment C
Transects	A, B, C (E*)	C (W*), D (SE*)	D (NW*)
Relative position	North and East of FHP.	South of southeastern end of FHP	West
Resistivity pattern	High resistivities (/) with patches of very high resistivities occurring >10 m b.g.l.	Low resistivities in the deepest 15–25 m. (/) Moderate to high resistivities in the shallowest 25–35 m distributed in a complex pattern. Low resistivities reach near the surface at the boundary to segment II.	Very low resistivities in the top gradually increasing to low resistivities at the base.
Resistivity range	1000–5000 Ωm / 5000–50000 Ωm	20–100 Ωm / 500–5000 Ωm	1.8–50 Ωm

232 *Compass directions in brackets indicate when only that part of transect belongs to the segment.

233 **Figure 4** (next page) Resistivity models of ERT transects produced by the inversion with ResIPy
 234 3.0.1 (Blanchy et al., 2020) and log-sensitivity of these resistivity models. Log-sensitivity values
 235 below zero (blue colors) indicate that the predicted resistivities are poorly constrained by the
 236 measurements while higher values (red colors) indicate better constrain. The insert at the bottom
 237 shows the location of the transects (see also Figure 3). The number of iterations and final root-
 238 mean-square error (RMSE) are written in the lower left corner of each transect. Based on the
 239 observed resistivities, we divided the transects into three segments. A description of these are
 240 summarized in Table 1.

241



243 **5 Discussion - Implications of resistivity models**

244 Indicating a robust inversion, log-sensitivity values above zero dominated the majority of
245 the resistivity models (Figure 4) and suggested that most of the predicted values represent true
246 ground conditions. However, the low sensitivities dominating Segment III indicated that the
247 resistivity values predicted here should be interpreted with greater caution. When low resistivity
248 values dominate shallow ground conditions, the depth of current flow is reduced and
249 measurements are thus less sensitive to deeper layers of the subsurface (Binley, 2015). For
250 Segment III, this implied that the predicted low resistivities may conceal zones of higher
251 resistivities. To quantify this potential concealment, we conducted a series of forward modelling
252 experiments with ResIPy, which are described in detail in the Supporting Information (Text S2).
253 From these experiments, we conclude that low resistivities dominate at least the shallowest 15 m
254 b.g.l. and likely extent to more than 25 m b.g.l.

255 The relatively strong differences observed on the resistivity models surrounding FHP
256 (Figure 4) indicate varying conditions in the subsurface. In the following, we consider salinity,
257 lithology and phase of state as possible explanations for these differences.

258 Completely unfrozen ground could not explain the low resistivities in Segment III (Figure
259 4), because of the known occurrence of permafrost and the fact that the low resistivities
260 completely dominate the ground, rather than appearing as zones or patches within higher
261 resistivity values. Instead, we attributed the low resistivities of segment III to the Holocene
262 marine sediments of which FHP is also composed (Yoshikawa & Harada, 1995). Although such
263 low resistivities (1.8–50 Ωm , Figure 4) would not be expected for most permafrost environments
264 (e.g., Draebing & Eichel, 2017; Lewkowicz et al., 2011; Sjöberg et al., 2015), they are consistent
265 with previous measurements of marine sediments in Adventdalen (Harada & Yoshikawa, 1996;
266 Keating et al., 2018; Ross et al., 2007). Laboratory experiments of saline permafrost soils also
267 show similar resistivities (Y. Wu et al., 2017), although the difference in scale makes this
268 comparison less confident. We infer that an unfrozen saline water content of <5% documented in
269 other parts of Adventdalen (Gilbert et al., 2019; Keating et al., 2018) likely also explains the low
270 resistivities of Segment III.

271 The high and very high resistivities measured on the other side of FHP (Segment I,
272 Figure 4, Table 1) did not comply with the above explanation. Instead, the modelled values
273 (1000–50000 Ωm) pointed to permafrost with a limited unfrozen water content (Kneisel &
274 Hauck, 2008) and as such would be difficult to explain if the ground consisted of the
275 aforementioned marine sediments. We instead interpret the high resistivities to reflect a different
276 lithology, which, given the geological context, is likely to be shale or mudstone (Figure 2b). The
277 quite significant resistivity range may have resulted from differences in fracture abundance,
278 lithological differences or differences in ground ice concentration, but borehole calibration or
279 other investigations are needed before an unequivocal interpretation can be made.

280 Constituting the transition between Segments I and III, and thus two different lithologies,
281 Segment II presumably spans a geological boundary. At the same time, this segment passes
282 closely to recent spring locations that may affect subsurface thermal regimes and influence
283 subsurface resistivities. As such, the moderate to high resistivities distributed heterogeneously
284 throughout the segment are likely explained as zones with high ice concentrations. This view is
285 consistent with ERT surveys of the internal structures of Longyear and Førstehytte Pingos that
286 documented similar complex resistivity patterns (Ross et al., 2007). Ross et al.'s (2007) ERT

287 survey at FHP resulted in a 175 m long profile running in a NE-SW direction along the crest of
288 the pingo (Figure 3). We digitized this profile and present it along with our own survey results in
289 a 3D animation, which, to our knowledge, shows all ERT transects from FHP (link to 3D
290 animation).

291 As for our survey, different lithologies and groundwater salinities often characterize the
292 ground in coastal environments. This results in electrical resistivity contrasts that may not
293 correlate with the distribution of frozen and unfrozen ground, and interpretations of frozen and
294 unfrozen ground state may thus be challenging. However, as this survey also shows, electrical
295 resistivity contrasts controlled by salinity and lithology may be increased as permafrost becomes
296 established, and electrical surveys will consequently be able to detect these contrasts more easily.

297 From the above interpretation, we see that FHP is located exactly at the boundary
298 between the consolidated bedrock and the marine valley infill. Assuming that this is not a
299 coincidental conjunction, one needs to consider the geological boundary when explaining the
300 location of FHP. The conjunction might be explained by groundwater recharge in the adjacent
301 highlands discharging at the foothill. However, such explanation would not be consistent with
302 the high electrical ground resistivities found towards the mountainside. Instead, the conjunction
303 of FHP and the geological boundary is in line with the aforementioned conceptual model (Figure
304 1) that glacially induced fractures in the sedimentary bedrock comprise a hydrological pathway
305 for deep groundwater to reach the surface. This view is supported by the geochemistry of pingo
306 spring waters in Adventdalen, which indicates a deep groundwater origin (Hodson et al., 2020;
307 Hornum et al., 2020).

308 To our knowledge, no other investigation at any of the open-system pingos in Svalbard
309 that are found along valley flanks (e.g., Humlum et al., 2003) have mapped the geological
310 context in detail. Still, we hypothesise that a similar mechanism may also contribute to the
311 formation of some of the open-system pingos found in Svalbard in similar geological contexts.
312 This would readily explain for example the elongated shapes of LP and FHP and their alignment
313 with the valley flank.

314 **6 Conclusions**

315 This study is the first to show a direct relationship between a geological boundary and an
316 open-system pingo. The strong electrical resistivity contrast observed between the uphill and
317 valley sides of Førstehytte Pingo likely reflects a lithological difference: the high resistivities
318 observed towards the mountainside are consistent with frozen sedimentary rocks with a limited
319 groundwater content, while permafrost with a low but saline content of groundwater explains the
320 low resistivities on the valley-side. Groundwater presumably flows flow to the pingo springs
321 through fractures in the sedimentary bedrock induced during glacial loading and unloading. This
322 view is supported by spring water geochemistry that indicates a deep groundwater origin and by
323 the consistently high electrical ground resistivities towards the mountainside of FHP, which does
324 not favor a topographic groundwater source. The numerous pingos on Svalbard that also locate
325 along valley margins are possibly associated with this boundary as well, and if so, these are
326 explained by groundwater in glacial fractures. Our findings indicate that shallow fractures in the
327 Late Weichselian landscape relief may constitute a previously overlooked groundwater pathway.
328 The fracture zone may link deep groundwater systems to the surface, where low-permeable
329 sediments cover this surface. On a circumpolar scale, flanks of uplifted valleys deserve particular
330 attention as possible pathways for subsurface fluids.

331 **Acknowledgments**

332 This work was conducted within the Catchment Transport and Cryohydrology Network
333 (CatchNet) funded by the Swedish Nuclear Fuel and Waste Management Company (SKB), and
334 the CLIMAGAS project (Climate forcing of terrestrial methane gas escape through permafrost in
335 Svalbard) funded by the Research Council of Norway (grant no. NRC 294764). The authors
336 acknowledge Aart Kroon and Ylva Sjöberg for critical feedback and comments to an earlier
337 version of this manuscript. For help in the field, the authors thank Matt, Linn, Trine, Antoine,
338 Daniela, Erik and UNIS students of the AG340 course. The measured and inverted electrical
339 resistivity data supporting this research is public available from the Zenodo repository (Hornum,
340 2021).

341 **References**

- 342 Andersen, D. T., Pollard, W. H., McKay, C. P., & Heldmann, J. (2002). Cold springs in
343 permafrost on Earth and Mars. *Journal of Geophysical Research E: Planets*, 107(3).
344 <https://doi.org/10.1029/2000je001436>
- 345 Ballantyne, C. K. (2018). *Periglacial geomorphology*. Hoboken, New Jersey, USA: John Wiley
346 & Sons Ltd.
- 347 Binley, A. (2015). Tools and Techniques: Electrical Methods. In G. Schubert (Ed.), *Treatise on*
348 *Geophysics* (2nd ed., Vol. 11, pp. 233–259). Amsterdam, the Netherlands: Elsevier.
349 <https://doi.org/10.1016/B978-0-444-53802-4.00192-5>
- 350 Binley, A. (2019). *R2 version 4.0 (November 2019)*. Lancaster, England: Lancaster University.
351 Retrieved from http://www.es.lancs.ac.uk/people/amb/Freeware/R2/R2_readme.pdf
- 352 Binley, A., & Kemna, A. (2005). DC Resistivity and Induced Polarization Methods. In Y. Rubin
353 & S. S. Hubbard (Eds.), *Hydrogeophysics* (1st ed., Vol. 50, pp. 129–156). New York, USA:
354 Springer. <https://doi.org/10.1007/1-4020-3102-5>
- 355 Blanchy, G., Saneiyani, S., Boyd, J., McLachlan, P., & Binley, A. (2020). ResIPy, an intuitive
356 open source software for complex geoelectrical inversion/modeling. *Computers and*
357 *Geosciences*, 137(104423). <https://doi.org/10.1016/j.cageo.2020.104423>
- 358 Christiansen, H. H., French, H. M., & Humlum, O. (2005). Permafrost in the Gruve-7 mine,
359 Adventdalen, Svalbard. *Norsk Geografisk Tidsskrift*, 59(2), 109–115.
360 <https://doi.org/10.1080/00291950510020592>
- 361 Cochand, M., Molson, J., & Lemieux, J. M. (2019). Groundwater hydrogeochemistry in
362 permafrost regions. *Permafrost and Periglacial Processes*, 30(2), 90–103.
363 <https://doi.org/10.1002/ppp.1998>
- 364 Draebing, D., & Eichel, J. (2017). Spatial Controls of Turf-Banked Solifluction Lobes and Their
365 Role for Paraglacial Adjustment in Glacier Forelands. *Permafrost and Periglacial*
366 *Processes*, 28(2), 446–459. <https://doi.org/10.1002/ppp.1930>
- 367 Fitts, C. R. (2002). *Groundwater Science*. *Groundwater Science* (1st ed.). Cambridge, MA,
368 USA: Academic Press. <https://doi.org/10.1016/C2009-0-62950-0>
- 369 French, H. M. (2017). *The Periglacial Environment* (4th ed.). Hoboken, New Jersey, USA: John
370 Wiley & Sons Ltd.

371 Gilbert, G. L., O'Neill, H. B., Nemec, W., Thiel, C., Christiansen, H. H., & Buylaert, J. P.
372 (2018). Late Quaternary sedimentation and permafrost development in a Svalbard fjord-
373 valley, Norwegian high Arctic. *Sedimentology*, 65(7), 2531–2558.
374 <https://doi.org/10.1111/sed.12476>

375 Gilbert, G. L., Instanes, A., O. Sinitsyn, A., & Aalberg, A. (2019). Characterization of two sites
376 for geotechnical testing in permafrost: Longyearbyen, Svalbard. *AIMS Geosciences*, 5(4),
377 868–885. <https://doi.org/10.3934/geosci.2019.4.868>

378 Gilichinsky, D., Rivkina, E., Shcherbakova, V., Laurinavichuis, K., & Tiedje, J. (2003).
379 Supercooled water brines within permafrost - An unknown ecological niche for
380 microorganisms: A model for astrobiology. *Astrobiology*, 3(2), 331–341.
381 <https://doi.org/10.1089/153110703769016424>

382 Grasby, S. E., Beauchamp, B., & Bense, V. (2012). Sulfuric acid speleogenesis associated with a
383 glacially driven groundwater system-paleo-spring “pipes” at Borup Fiord Pass, Nunavut.
384 *Astrobiology*, 12(1), 19–28. <https://doi.org/10.1089/ast.2011.0700>

385 Grosse, G., Goetz, S., McGuire, A. D., Romanovsky, V. E., & Schuur, E. A. G. (2016).
386 Changing permafrost in a warming world and feedbacks to the Earth system. *Environmental*
387 *Research Letters*, 11, 040201. <https://doi.org/10.1088/1748-9326/11/4/040201>

388 Haldorsen, S., Heim, M., & Lauritzen, S. E. (1996). Subpermafrost Groundwater, Western
389 Svalbard. *Nordic Hydrology*, 27(1–2), 57–68. <https://doi.org/10.2166/nh.1996.0019>

390 Harada, K., & Yoshikawa, K. (1996). Permafrost age and thickness near Adventfjorden,
391 Spitsbergen. *Polar Geography*, 20(4), 267–281.
392 <https://doi.org/10.1080/10889379609377607>

393 Hodson, A., Nowak, A., Redeker, K. R., Holmlund, E. S., Christiansen, H. H., & Turchyn, A. V.
394 (2019). Seasonal dynamics of methane and carbon dioxide evasion from an open system
395 pingo: Lagoon pingo, svalbard. *Frontiers in Earth Science*, 7, 30.
396 <https://doi.org/10.3389/feart.2019.00030>

397 Hodson, A., Nowak, A., Hornum, M. T., Senger, K., Redeker, K. R., Christiansen, H. H., et al.
398 (2020). Sub-permafrost methane seepage from open-system pingos in Svalbard. *The*
399 *Cryosphere*, 14, 3829–3842. <https://doi.org/10.5194/tc-14-3829-2020>

400 Hornum, M. T. (2021). ERT data from Førstehytte Pingo, Adventdalen, Svalbard. Zenodo.
401 [https://doi.org/DOI: 10.5281/zenodo.4479529](https://doi.org/DOI:10.5281/zenodo.4479529)

402 Hornum, M. T., Hodson, A., Jessen, S., Bense, V., & Senger, K. (2020). Numerical modelling of
403 permafrost spring discharge and open-system pingo formation induced by basal permafrost
404 aggradation. *The Cryosphere*, 14, 4627–4651. <https://doi.org/https://doi.org/10.5194/tc-14-4627-2020>

406 Humlum, O. (2005). Holocene permafrost aggradation in Svalbard. *Geological Society Special*
407 *Publication*, 242, 119–130. <https://doi.org/10.1144/GSL.SP.2005.242.01.11>

408 Humlum, O., Instanes, A., & Sollid, J. L. (2003). Permafrost in Svalbard: A review of research
409 history, climatic background and engineering challenges. *Polar Research*, 22(2), 191–215.
410 <https://doi.org/10.3402/polar.v22i2.6455>

411 Huq, F., Smalley, P. C., Mørkved, P. T., Johansen, I., Yarushina, V., & Johansen, H. (2017). The

- 412 Longyearbyen CO2 Lab: Fluid communication in reservoir and caprock. *International*
413 *Journal of Greenhouse Gas Control*, 63, 59–76. <https://doi.org/10.1016/j.ijggc.2017.05.005>
- 414 Keating, K., Binley, A., Bense, V., Van Dam, R. L., & Christiansen, H. H. (2018). Combined
415 Geophysical Measurements Provide Evidence for Unfrozen Water in Permafrost in the
416 Adventdalen Valley in Svalbard. *Geophysical Research Letters*, 45(15), 7606–7614.
417 <https://doi.org/10.1029/2017GL076508>
- 418 Kim, J. H., Supper, R., Ottowitz, D., Jochum, B., & Yi, M. J. (2016). A new measurement
419 protocol of direct current resistivity data. *Geophysics*, 81(2), A7–A11.
420 <https://doi.org/10.1190/GEO2015-0419.1>
- 421 Kneisel, C., & Hauck, C. (2008). Electrical methods. In C. Hauck & C. Kneisel (Eds.), *Applied*
422 *Geophysics in Periglacial Environments* (1st ed., pp. 3–27). Cambridge, England:
423 Cambridge University Press.
- 424 Kneisel, C., Hauck, C., Fortier, R., & Moorman, B. (2008). Advances in Geophysical Methods
425 for Permafrost Investigations. *Permafrost and Periglacial Processes*, 19, 157–178.
426 <https://doi.org/10.1002/ppp.616>
- 427 Leith, K., Moore, J. R., Amann, F., & Loew, S. (2014a). In situ stress control on microcrack
428 generation and macroscopic extensional fracture in exhuming bedrock. *Journal of*
429 *Geophysical Research: Solid Earth*, 119(1), 594–615.
430 <https://doi.org/10.1002/2012JB009801>
- 431 Leith, K., Moore, J. R., Amann, F., & Loew, S. (2014b). Subglacial extensional fracture
432 development and implications for Alpine Valley evolution. *Journal of Geophysical*
433 *Research: Earth Surface*, 119(1), 62–81. <https://doi.org/10.1002/2012JF002691>
- 434 Lewkowicz, A. G., Etzelmüller, B., & Smith, S. L. (2011). Characteristics of discontinuous
435 permafrost based on ground temperature measurements and electrical resistivity
436 tomography, Southern Yukon, Canada. *Permafrost and Periglacial Processes*, 22(4), 320–
437 342. <https://doi.org/10.1002/ppp.703>
- 438 Liestøl, O. (1977). Pingos, springs, and permafrost in Spitsbergen. In A. Brekke (Ed.), *Norsk*
439 *Polarinstitutt Årbok 1975* (pp. 7–29). Oslo, Norway: Universitetsforlaget.
- 440 Liestøl, O. (1996). Open-system pingos in Spitsbergen. *Norsk Geografisk Tidsskrift*, 50, 81–84.
441 <https://doi.org/10.1080/00291959608552355>
- 442 Mackay, J. R. (1998). Pingo growth and collapse, Tuktoyaktuk Peninsula area, western arctic
443 coast, Canada: A long-term field study. *Geographie Physique et Quaternaire*, 52(3), 271–
444 323. <https://doi.org/10.7202/004847ar>
- 445 Mangerud, J., & Svendsen, J. I. (2017). The Holocene Thermal Maximum around Svalbard,
446 Arctic North Atlantic; molluscs show early and exceptional warmth. *The Holocene*, 28(1),
447 65–83. <https://doi.org/10.1177/0959683617715701>
- 448 Minsley, B. J., Abraham, J. D., Smith, B. D., Cannia, J. C., Voss, C. I., Jorgenson, M. T., et al.
449 (2012). Airborne electromagnetic imaging of discontinuous permafrost. *Geophysical*
450 *Research Letters*, 39(L02503). <https://doi.org/10.1029/2011GL050079>
- 451 Neuzil, C. E. (2012). Hydromechanical effects of continental glaciation on groundwater systems.
452 *Geofluids*, 12(1), 22–37. <https://doi.org/10.1111/j.1468-8123.2011.00347.x>

- 453 Norwegian Polar Institute. (2020). Map data. Retrieved May 13, 2020, from
454 <https://geodata.npolar.no/>
- 455 Olausen, S., Senger, K., Braathen, A., Grundvåg, S.-A., & Mørk, A. (2020). You learn as long
456 as you drill; research synthesis from the Longyearbyen CO2 Laboratory, Svalbard, Norway.
457 *Norwegian Journal of Geology*, 99(2), 157–187. <https://doi.org/10.17850/njg008>
- 458 Palacky, G. J. (1988). Resistivity Characteristics of Geologic Targets. In M. N. Nabighian (Ed.),
459 *Electromagnetic Methods in Applied Geophysics* (Vol. 1: Theory, pp. 52–129). Tulsa,
460 Oklahoma: Society of Exploration Geophysicists.
461 <https://doi.org/10.1190/1.9781560802631.ch3>
- 462 Reynolds, J. M. (2011). *An Introduction to Applied and Environmental Geophysics* (2nd ed.).
463 Hoboken, New Jersey, USA: John Wiley & Sons.
- 464 Ross, N., Brabham, P. J., Harris, C., & Christiansen, H. H. (2007). Internal structure of open
465 system pingos, adventdalen, svalbard: The use of resistivity tomography to assess ground-
466 ice conditions. *Journal of Environmental and Engineering Geophysics*, 12(1), 113–126.
467 <https://doi.org/10.2113/JEEG12.1.113>
- 468 Rossi, G., Accaino, F., Boaga, J., Petronio, L., Romeo, R., & Wheeler, W. (2018). Seismic
469 survey on an open pingo system in Adventdalen Valley, Spitsbergen, Svalbard. *Near*
470 *Surface Geophysics*, 16(1), 89–103. <https://doi.org/10.3997/1873-0604.2017037>
- 471 Scheidegger, J. M., & Bense, V. F. (2014). Impacts of glacially recharged groundwater flow
472 systems on talik evolution. *Journal of Geophysical Research: Earth Surface*, 119(4), 758–
473 778. <https://doi.org/10.1002/2013JF002894>
- 474 Scheidegger, J. M., Bense, V. F., & Grasby, S. E. (2012). Transient nature of Arctic spring
475 systems driven by subglacial meltwater. *Geophysical Research Letters*, 39(12), 1–6.
476 <https://doi.org/10.1029/2012GL051445>
- 477 Scholz, H., & Baumann, M. (1997). An 'open system pingo' near Kangerlussuaq (Søndre
478 Strømfjord), West Greenland. *Geology of Greenland Survey Bulletin*, 176, 104–108.
479 <https://doi.org/https://doi.org/10.34194/ggub.v176.5074>
- 480 Schuster, P. F., Schaefer, K. M., Aiken, G. R., Antweiler, R. C., Dewild, J. F., Gryziec, J. D., et
481 al. (2018). Permafrost Stores a Globally Significant Amount of Mercury. *Geophysical*
482 *Research Letters*, 45(3), 1463–1471. <https://doi.org/10.1002/2017GL075571>
- 483 Scott, W. J., Sellmann, P. V., & Hunter, J. A. (1990). Geophysics in the Study of Permafrost. In
484 S. H. Ward (Ed.), *Geotechnical and Environmental Geophysics* (Vol. 1, pp. 355–384).
485 Tulsa, Oklahoma: Society of Exploration Geophysicists.
486 <https://doi.org/https://doi.org/10.1190/1.9781560802785.ch13>
- 487 Sjöberg, Y., Marklund, P., Pettersson, R., & Lyon, S. W. (2015). Geophysical mapping of palsa
488 peatland permafrost. *Cryosphere*, 9(2), 465–478. <https://doi.org/10.5194/tc-9-465-2015>
- 489 Williams, J. R. (1970). *Ground Water in the Permafrost Regions of Alaska*. USGS Professional
490 *Paper 696*. Reston, Virginia, USA. <https://doi.org/https://doi.org/10.3133/pp696>
- 491 Wu, Y., Nakagawa, S., Kneafsey, T. J., Dafflon, B., & Hubbard, S. (2017). Electrical and
492 seismic response of saline permafrost soil during freeze - Thaw transition. *Journal of*
493 *Applied Geophysics*, 146, 16–26. <https://doi.org/10.1016/j.jappgeo.2017.08.008>

- 494 Wu, Z., Barosh, P. J., Hu, D., Wu, Z., Peisheng, Y., Qisheng, L., & Chunjing, Z. (2005).
495 Migrating pingos in the permafrost region of the Tibetan Plateau, China and their hazard
496 along the Golmud-Lhasa railway. *Engineering Geology*, 79, 267–287.
497 <https://doi.org/10.1016/j.enggeo.2005.02.003>
- 498 Yoshikawa, K. (1993). Notes on open-system pingo ice, Adventdalen, Spitsbergen. *Permafrost*
499 *and Periglacial Processes*, 4(4), 327–334. <https://doi.org/10.1002/ppp.3430040405>
- 500 Yoshikawa, K. (2013). Pingos. In J. Shroder, R. Giardino, & J. Harbor (Eds.), *Treatise on*
501 *Geomorphology* (Vol. 8, pp. 274–297). San Diego, California, USA: Academic Press.
502 <https://doi.org/10.1016/B978-0-12-374739-6.00212-8>
- 503 Yoshikawa, K., & Harada, K. (1995). Observations on nearshore pingo growth, Adventdalen,
504 Spitsbergen. *Permafrost and Periglacial Processes*, 6(4), 361–372.
505 <https://doi.org/10.1002/ppp.3430060407>
- 506 Yoshikawa, K., & Nakamura, T. (1996). Pingo growth ages in the delta area, Adventdalen,
507 Spitsbergen. *Polar Record*, 32(183), 347–352. <https://doi.org/10.1017/S0032247400067565>